Bright quantum dots emitting at ~1,600 nm in the NIR-IIb window for deep tissue fluorescence imaging

Mingxi Zhang[a,b,1], Jingying Yue[a,1], Ran Cui[a,c,1], Zhuoran Ma[a,1], Hao Wan[a,1], Feifei Wang[a], Shoujun Zhu[a], Ying Zhou[a], Yun Kuang[a], Yeteng Zhong[a], Dai-Wen Pang[c], and Hongjie Dai[a,2]

[a]Department of Chemistry, Stanford University, Stanford, CA 94305; [b]State Key Laboratory of Advanced Technology for Materials Synthesis and Processing, Wuhan University of Technology, 430070 Wuhan, China; and [c]Key Laboratory of Analytical Chemistry for Biology and Medicine (Ministry of Education), College of Chemistry and Molecular Sciences, Wuhan University, 430072 Wuhan, China

With suppressed photon scattering and diminished autofluorescence, in vivo fluorescence imaging in the 1,500- to 1,700-nm range of the near-IR (NIR) spectrum (NIR-IIb window) can afford high clarity and deep tissue penetration. However, there has been a lack of NIR-IIb fluorescent probes with sufficient brightness and aqueous stability. Here, we present a bright fluorescent probe emitting at ~1,600 nm based on core/shell lead sulfide/cadmium sulfide (CdS) quantum dots (CSQDs) synthesized in organic phase. The CdS shell plays a critical role of protecting the lead sulfide (PbS) core from oxidation and retaining its bright fluorescence through the process of amphiphilic polymer coating and transferring to water needed for imparting aqueous stability and compatibility. The resulting CSQDs with a branched PEG outer layer exhibited a long blood circulation half-life of 7 hours and enabled through-skin, real-time imaging of blood flows in mouse vasculatures at an unprecedented 60 frames per second (fps) speed by detecting ~1,600-nm fluorescence under 808-nm excitation. It also allowed through-skin in vivo confocal 3D imaging of tumor vasculatures in mice with an imaging depth of ~1.2 mm. The PEG-CSQDs accumulated in tumor effectively through the enhanced permeation and retention effect, affording a high tumor-to-normal tissue ratio up to ~32 owing to the bright ~1,600-nm emission and nearly zero autofluorescence background resulting from a large ~800-nm Stoke's shift. The aqueous-compatible CSQDs are excreted through the biliary pathway without causing obvious toxicity effects, suggesting a useful class of ~1,600-nm emitting probes for biomedical research.

fluorescence imaging | in vivo | NIR-IIb window | quantum dots | deep tissue

Fluorescence imaging of biological tissues in vivo or ex vivo can provide direct visualization of biological structures and functions with high spatial and temporal resolution (1, 2). Recently, we and others have shown that fluorescent probes emitting in the second near-IR (NIR; NIR-II, 1,000–1,700 nm) can facilitate deeper tissue fluorescence imaging than previously done in NIR-I (~800–900 nm) by taking advantage of suppressed tissue scattering of longer wavelength-emitted light and diminished autofluorescence background in this region (3–23). Several classes of NIR-II fluorescent probes have been developed and deployed for blood hemodynamics visualization (8, 17), cerebrovascular imaging (10, 18), and tumor targeting (11, 16, 23). However, brighter probes and probes emitting at longer wavelengths are still urgently needed to push the limit of in vivo fluorescence imaging clarity and penetration depth.

Imaging in the long end of the NIR-II 1,000- to 1,700-nm wavelength range [i.e., in the NIR-IIb window (namely 1,500–1,700 nm)] can minimize photon scattering and still avoid high absorbance by water in tissues, affording high resolution (approximately micrometers) of mouse vasculatures at several millimeter depths in the brain or other tissues (12). The ~1,600-nm region is located between water absorption overtone peaks and is well-suited for deep tissue optical imaging (Fig. 1D). Beyond 1,700 nm, water absorption increases accompanied by the loss of sensitivity of

indium gallium arsenide (InGaAs) detectors used for NIR-II imaging in 1,000–1,700 nm, making imaging difficult despite further reduced light scattering. To date, only a few NIR-IIb fluorescence probes have been developed for in vivo imaging, including laser vaporization-derived, single-walled carbon nanotubes [quantum yield (QY): ~0.01%] (12), rare earth down-conversion nanocrystals (QY: ~0.27–2.73%) (14, 20, 24, 25), and indium arsenide-based quantum dots (QDs; QY: ~5%) (15). Clearly, more types and brighter probes are needed in this important wavelength range.

Lead sulfide (PbS) QDs have attracted much attention over the years for optical and optoelectronic applications owing to their narrow bandgap and larger Bohr's radii with respect to other QDs (26–28). The strong and tunable emission spanning the entire NIR-II window makes it a highly promising candidate for in vivo imaging (29). However, the optical properties of PbS QDs are prone to surface oxidation or other reactions in various environments, including aqueous dispersion media (30), or in thin film optical devices (31). The fluorescence intensity and photostability of PbS QDs are dramatically decreased on transferring to aqueous solutions. This was a problem encountered by our group after the first mouse NIR-II imaging work based on carbon nanotubes (6) in an effort to explore brighter NIR-II probes. In the optical device field, higher-performance photovoltaic and light-emitting devices (32–34) have been obtained by using cadmium sulfide (CdS) as a protection layer to the PbS core against oxidation and as a better passivation layer to remove surface defects/traps. In the chemistry and biological application area, several groups performed

Significance

In vivo fluorescence imaging in near IR-IIb window (1,500–1,700 nm) can provide high spatial and temporal resolution and deep tissue penetration for fundamental research and potential translations. Herein, a bright fluorescent probe emitting at ~1,600 nm based on lead sulfide (PbS)/CdS quantum dots was developed. The CdS shell helped to chemically passivate and retain the high fluorescence of the PbS core after phase transfer to aqueous solutions for biocompatibility. The 1,600-nm emitting probe allowed noninvasive, millimeter-deep fluorescence imaging at high speeds up to 60 frames per second with micrometer-scale spatial resolution in 2D wide-field and 3D confocal modes. The probes were nontoxic and largely excreted over 1 month, providing a tool for in vivo research of preclinical animal models.
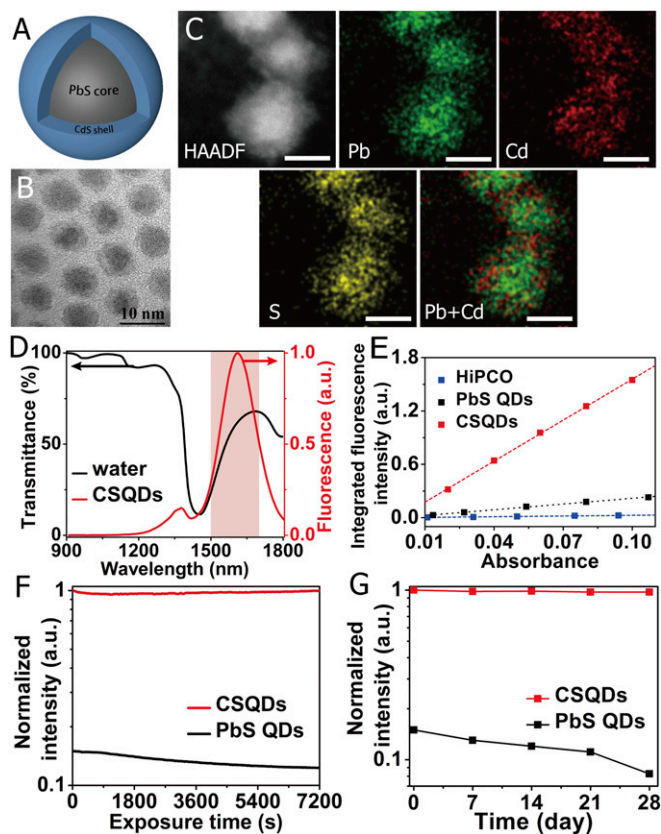
Fig. 1. Characterization of NIR-IIb–emitting CSQDs. (*A*) Schematic design of CSQDs. (*B*) TEM image and high-resolution TEM image of as-prepared PbS/CdS QDs. (Scale bar: 10 nm.) (*C*) HAADF-STEM images of the PbS/CdS core/shell nanostructure. The energy-dispersive X-ray spectroscopy elemental maps show the distribution of Pb (green), Cd (red), and S (yellow). (Scale bar: 5 nm.) (*D*) Fluorescence emission spectrum of PEGylated CSQDs (right axis) plotted together with water transmittance spectrum (left axis). The pink region highlights the NIR-IIb window. (*E*) Plot of the integrated fluorescence spectra of PEG-CSQDs, PEGylated PbS QDs, and HiPCO-SWNTs at five different absorbance values of 808 nm or concentrations. Linear fits were used to calculate quantum yield by comparing the slopes with reference HiPCO-SWNTs (QY ∼ 0.04–0.4%). (*F*) Photostability of PEGylated PbS QDs and PbS/CdS CSQDs in PBS under continuous 808-nm laser exposure for 2 h. The *y* axis shows the fluorescence intensity of the samples normalized to CSQD. (*G*) The long-time stability of PEGylated PbS QDs and PbS/CdS CSQDs in PBS at 4 °C over the course of 4 wk. The *y* axis shows the fluorescence intensity of the samples normalized to CSQD.

fluorescence imaging in the 1,000- to 1,400-nm region using less bright PbS QDs without surface passivation (35, 36). CdS shell was used to circumvent the aqueous quenching problem for PbS QDs emitting in the 1,000- to 1,400-nm range (37, 38) but not longer wavelengths to further minimize tissue scattering.

Here, we synthesized core/shell lead sulfide/CdS quantum dots (CSQDs) emitting at ∼1,600 nm and utilized the CdS coating shell to protect the PbS core from reactions/degradation, thus retaining the high fluorescence of the PbS core after PEGylation and phase transfer to aqueous solutions. The bright CSQDs enabled in vivo imaging of ∼1,600-nm fluorescence in NIR-IIb under 808-nm excitation using short exposure times down to 2–5 ms, allowing for fast, real-time imaging of blood flows at frame rates of 60 frames per second (fps). This represented the fastest NIR-II imaging speed to date in 1,000–1,700 nm with any fluorescent probes. Through-skin in vivo 3D confocal imaging of tumor vasculature with a depth of ∼1.2 mm was achieved with CSQDs. Moreover, in vivo imaging of mouse tumor with CSQDs through the enhanced permeation and retention effect was shown in the

NIR-IIb window, outperforming other NIR probes with a superior tumor-to-normal tissue (T/NT) ratio up to 32.

Results and Discussion

Synthesis and Phase Transfer of PbS/CdS CSQDs. CSQDs synthesis involved tuning the core shell structure through controlling the PbS core size to ∼5.4 nm for ∼1,600-nm emission, forming an ∼1.5-nm-thick CdS shell and developing suitable surface chemical coating for stable aqueous transfer and biocompatibility. It started with synthesis of oleic acid-capped PbS QDs by using a modified method reported previously (39, 40). Then, a low-temperature Pb to Cd cation exchange procedure was optimized to produce the CSQDs (Fig. 1*A*) with minimal Ostwald ripening and a high degree of size uniformity (*SI Appendix, Materials and Methods*) (41, 42). The as-prepared QDs were uniform with a narrow size distribution (6.9 ± 0.4 nm) from transmission EM (TEM) (*SI Appendix*, Fig. S1). A layer of outer shell with a thickness of 1.5 ± 0.2 nm was identified in the high-resolution TEM images (Fig. 1*B*). Successful cation exchange was evidenced by elemental mapping (Fig. 1*C*) using high-angle annular dark-field scanning transmission EM (HAADF-STEM) and energy-dispersive X-ray spectroscopy (*SI Appendix*, Fig. S2*A*). As shown in *SI Appendix*, Fig. S2*B*, all peaks in the powder X-ray diffraction spectra of PbS QDs and the corresponding CSQDs could be indexed to PbS face-centered cubic pattern (Joint Committee Powder Diffraction Standards 5–0592). However, broadened and red-shifted peaks of PbS/CdS CSQDs were observed due to the nanoscale PbS core and formation of CdS shell leading to overlap and red shift of diffraction peaks (43). Comparing the fluorescence spectra of PbS QDs and PbS/CdS CSQDs taken in trichloroethylene (*SI Appendix*, Fig. S3), we observed a blue shift from 1,725 nm of pure PbS QDs to 1,650 nm of PbS/CdS QDs, consistent with the reduced PbS core size on the formation of CdS shell by cation exchange.

For surface modification of CSQDs (44), an amphiphilic polymer, oleyamine-branched polyacrylic acid (OPA), was synthesized and served as an efficient coating layer (*SI Appendix* has synthesis and modification details) (45). When the OPA polymer was mixed with CSQDs in the organic phase, the hydrophobic tails of the polymer intercalated with alkyl chains of oleic acid on the surface of QDs and then formed ordered and compacted structure via van der Waals/hydrophobic interactions between multiple alkyl chains. The abundant carboxylic groups along the OPA polymer backbone allowed for the dispersion of CSQDs in aqueous solution and presented functional groups for further conjugation. To increase the biocompatibility of CSQDs for in vivo use, we screened and optimized a mixture of linear methoxypolyethylene glycol amine (molecular mass ∼5 kDa) and branched eight-arm polyethylene glycol amine (molecular mass ∼40 kDa) at a 24:1 molar ratio to PEGylate the OPA-modified products via 1-(3-dimethylaminopropyl)-3-ethylcarbodiimide hydrochloride chemistry. The TEM image showed that the as-prepared PEGylated lead sulfide/CdS core/shell lead sulfide/CdS quantum dots (PEG-CSQDs) were readily dispersed in buffer solution without negligible aggregation (*SI Appendix*, Fig. S4). Dynamic light scattering (DLS) revealed that the fully hydrated, hydrodynamic size of the resulting PEG-CSQDs in PBS was ∼18.2 nm. In addition, the DLS curve of PEG-CSQDs in FCS almost coincided with that in PBS (*SI Appendix*, Fig. S5), confirming that the PEG layer was able to prevent serum protein binding.

Fluorescence Properties of PEGylated CSQDs. We characterized the PEGylated CSQD in aqueous solutions and compared its optical properties with its analog PEGylated PbS QDs without CdS shell. As shown in Fig. 1*D*, the PEG-CSQDs dispersed in PBS showed an emission peak at 1,650 nm under an 808-nm laser excitation, falling in the 1,500- to 1,700-nm NIR-IIb region around a local minimum of water vibration overtone peaks. In PBS buffer solution (under 808-nm excitation), the CdS protection layer resulted in an approximately six to seven times brighter fluorescence than PbS QDs (without the CdS shell) that underwent the same surface coating and phase transfer process. The PEG-CSQDs were ∼55 times

Zhang et al.

CHEMISTRY

brighter than high-pressure carbon monoxide conversion single-walled nanotubes (HiPCO-SWNTs) with a QY of 2.2–22% (red curve in Fig. 1*E*) [referenced to 4-(7-(2-phenyl-4H-1-benzothio-pyran-4-ylidene)-4-chloro-3,5-trimethylene-1,3,5-heptatrienyl)-2-phenyl-1-benzothiopyrylium perchlorate (known as IR-26 dye) 0.05–0.5% QY] (46, 47), suggesting a bright fluorescent probe in the NIR-IIb region.

Excellent photostability of the PEG-CSQDs in PBS was observed in a 2-h continuous exposure test under an 808-nm laser at 60 mW/cm^2 (red curve in Fig. 1*F*). In addition, after storing at 4 °C for 4 wk, the PEG-CSQDs still kept their strong brightness without obvious decay (red curve in Fig. 1*G*). In contrast, the QY of PEGylated PbS QDs was only 0.33–3.3% to start with (black curve in Fig. 1*E*) and suffered a further decay by ∼20% after 2-h laser exposure (black curve in Fig. 1*F*). Moreover, further fluorescence decay (∼40%) occurred for PEGylated PbS QDs after long-time storage (black curve in Fig. 1*G*). These results confirmed that the CdS outer shell can effectively protect the PbS core from chemical and photochemical degradation effects, imparting excellent fluorescence properties and stability of QDs in aqueous solutions.

Fast, Real-Time Fluorescence Imaging at ∼1,600 nm in Vivo. Using 808-nm laser excitation (∼70 mW/cm^2), an InGaAs camera sensitive to photons up to ∼1,700 nm, and a 1,500-nm long-pass filter, we performed noninvasive in vivo imaging of blood vessels by detecting ∼1,600-nm fluorescence emitting from i.v. injected PEG-CSQDs (200 μL, 2 mg/mL) circulating in the mouse vasculature system. Reduced tissue scattering of photons in the NIR-IIb window by tissues allowed clear imaging of blood vessels inside hind limbs after injection of PEG-CSQD (Fig. 2*A*). The high brightness of PEG-CSQD allowed for real-time (defined as speed of >30 fps) imaging with exposure times down to ∼2–5 ms for hemodynamic tracking of blood flow in individual vessels (*SI Appendix*, Figs. S6 and S7 and Movies S2 and S3 show 2-ms imaging data). Immediately after tail vein injection of PEG-CSQD, NIR-IIb signal propagation with the blood flow in mouse hind limb vessels was recorded at a frame rate of 60 fps (Movie S1, temporal resolution of 16.7 ms). Note that we did not perform faster imaging due to the limited frame rate imposed by the camera at the desired gain setting. Previously, short exposure time of ∼2 ms was only shown in the <1,300-nm range using a donor–acceptor–donor probe at a maximum speed of ∼30 fps (23). Shortly after injection, we observed NIR-IIb fluorescence returning from the arterial flow into the femoral vein adjacent to the femoral artery (Fig. 2*A*, *t* = 0 defined as the time when signal started to appear in the femoral vein), clearly resolving the closely spaced femoral artery and vein (at ∼320-μm distance) (Fig. 2 *B–D*) at ∼2-mm depth inside the hind limb tissue. Principal component analysis (PCA) (9) was performed on the video rate images to clearly differentiate the arterial component from the venous component of the femoral vein (Fig. 2*B*, arterial component color-coded in red and venous component color-coded in blue).

NIR-IIb signal propagations in the hind limb were analyzed (Movie S1). By plotting the distance traveled by the flow front as a function of time, the average blood flow velocity of the femoral vein (indicated by the blue arrow in Fig. 2*B*) showed an overall linear increase, with an average blood velocity of ∼11.7 mm/s (Fig. 2*E*). The blood flow was accompanied by periodic changes in the fluorescence signal (Fig. 2*F*) corresponding to the ventricular ejection/relaxation phases of cardiac cycles (Movie S1 shows clear pulsing behavior of blood flow in the femoral vein). An average of 455.7 ms per pulse (∼27 frames per pulse) was obtained by plotting the time of periodic variation over pulses through linear fitting (Fig. 2*G*).

In Vivo Noninvasive Imaging of Tumor in NIR-IIb Window. Tumor imaging of tumor is of importance to both diagnostics and therapy for combating cancer and increasing survival rate. Molecular probes or nanostructures could accumulate in tumor due to the enhanced permeability and retention effect, which could be utilized for tumor imaging and identifying patients who could potentially benefit from nanoparticle-based drug delivery or therapy (48–50). On i.v. injection into C57BL/6 mice with xenograft MC38 tumors,
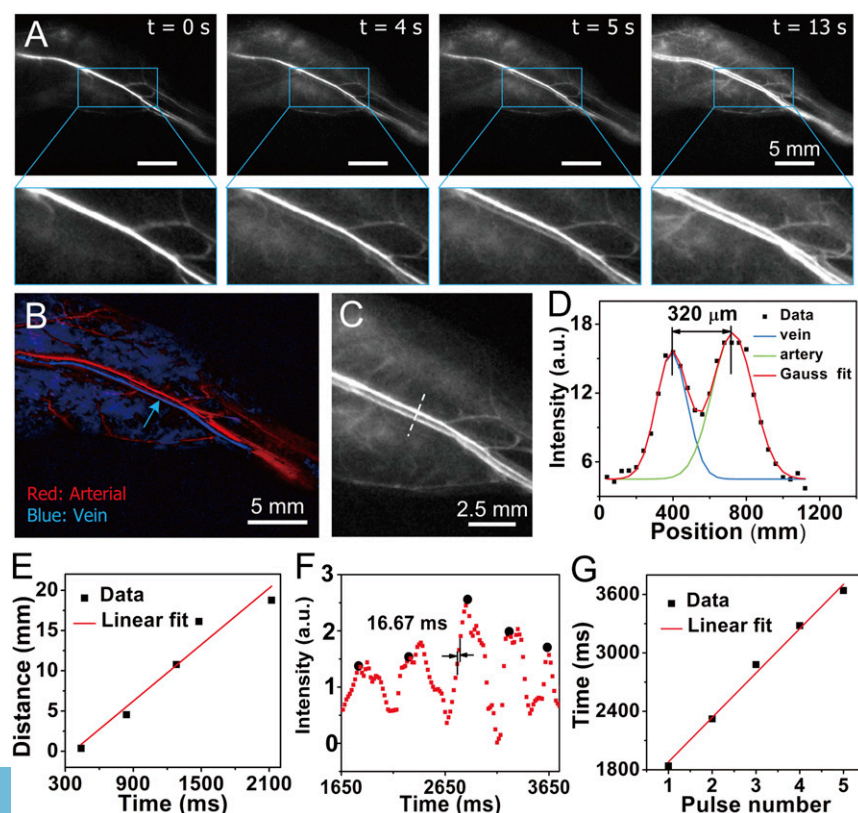

Fig. 2. Fast NIR-IIb imaging of blood flow in the NIR-IIb window at 60 fps. (*A*) A time course of ∼1,600-nm fluorescence images recorded at 808-nm excitation of a mouse hind limb after i.v. injection of PEG-CSQDs showing the blood flow returning to the femoral vein after filling the femoral artery; *t* = 0 is defined as the time point when NIR-IIb signal started to show up in the femoral vein. The frame rate of imaging is 60 fps (808-nm laser, 2.5× objective, 1,500-nm long-pass filter, 5-ms exposure time using a Ninox 640 InGaAs camera, laser power density ∼70 mW/cm^2). (Scale bar: 5 mm.) (*B*) PCA for differentiation of arterial and venous components. (*C*) A zoomed in image of a subregion in the hind limb. (*D*) Cross-sectional fluorescence intensity profile of femoral vein and artery marked in *C*. (*E*) Blood speed analysis in femoral vein. The calculated venous speed is 11.7 mm/s. (*F*) Periodic intensity oscillations of hind limb vessel. (*G*) Cardiac cycle analysis based on periodic variation over pulses. The calculated cardiac cycle is 455.7 mm per pulse.
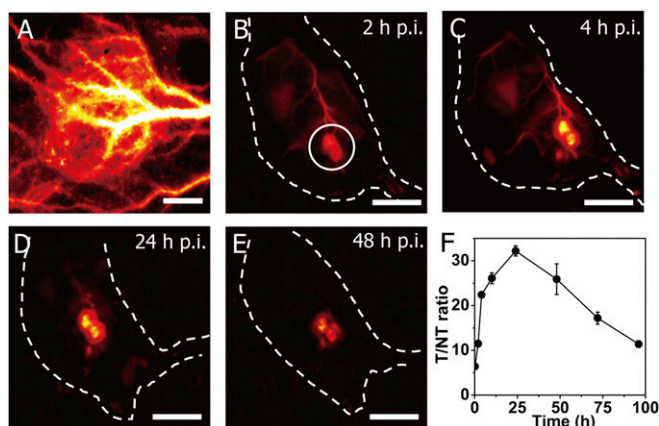
www.manaraa.com

Fig. 3. In vivo fluorescence imaging of tumor in the NIR-IIb window with a T/NT tissue ratio >30. (*A*) High-magnification (10× objective), wide-field fluorescence imaging (~1,600-nm emission, 808-nm excitation) of an s.c. xenograft MC38 tumor on a mouse after tail vein i.v. injection of PEG-CSQDs. (Scale bar: 1 mm.) (*B–E*) Wide-field fluorescence imaging (1× objective) at different time points after injection. (Scale bar: 10 mm.) (*F*) Time course curve of T/NT tissue ratios over the course of 96 h p.i. Wide-field imaging experiment parameters: 808-nm laser, 1,500-nm long-pass filter, laser power density ~60 mW/cm^2.

the PEG-CSQDs circulated over time and accumulated to a high degree to brightly light up the whole tumors (Fig. 3*A*). The high-magnification images showed that the PEG-CSQDs gradually leaked from vessels and diffused into tumor (*SI Appendix*, Fig. S8), which could be attributed to the structural abnormalities and the permeability increase of tumor vasculatures (51, 52). We continuously monitored the fluorescence change of tumor in the 1,500- to 1,700-nm range at different time points (Fig. 3 *B–E*) and calculated the T/NT signal ratios as a function of time (Fig. 3*F*). We observed that the T/NT ratio gradually increased and reached the peak at 24 h postinjection (p.i.) followed by a subsequent decrease over time. The highest T/NT ratio reached was ~32.6, which was the highest among all fluorescence-based tumor imaging with any fluorophores with or without molecular targeting. The accumulation of CSQDs within the tumor accompanied with extravasation of CSQD out of vessels also led to an increase of tumor-to-blood ratios as a function of time, reaching a peak value of ~6.7 at 48 h p.i (*SI Appendix*, Fig. S9). The high T/NT ratio of tumor imaging was attributed to the high brightness of PEG-CSQDs, the long circulation time for efficient enhanced permeation and retention, and the ultralow autofluorescence background by imaging with an unusually large ~800-nm Stoke's shift under an 808-nm excitation while detecting in the ~1,600-nm NIR-IIb window (53).

3D Confocal Imaging of Tumor in Vivo at ~1,600 nm. Recently, we built a one-photon confocal microscope for excitations in the 600- to 1,000-nm range and emission in the 1,000- to 1,700-nm range and showed one-photon confocal imaging of noncleared brain and other tissue samples ex vivo with penetration depths up to ~1.3 mm (22, 23). Here, the bright PEG-CSQDs were utilized to enable noninvasive, through-skin, high-resolution in vivo confocal imaging of mouse vasculatures several micrometers in diameter at millimeter depths (Fig. 4*A*). The confocal images of hind limb vasculatures of a C57BL/6 mouse shown in Fig. 4 *B* and *C* were acquired at resolutions of 10 and 2 μm, respectively. In a 300 × 300-μm image with a pixel size of 2 μm, a small vessel at a depth of ~270 μm was resolved in vivo with a high signal-to-background ratio of 6.3 (Fig. 4*C*). By measuring the Gaussian-fitted FWHM of the cross-sectional intensity profile, we calculated the apparent width (i.e., FWHM) to be ~7.9 μm (Fig. 4*D*). Note that the mouse was alive and that the vessels remained
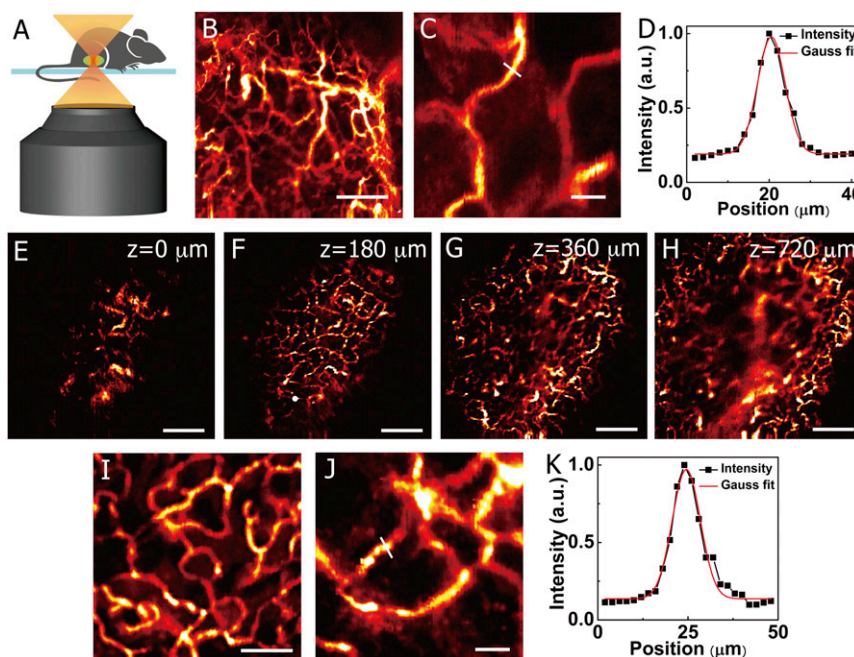

Fig. 4. In vivo noninvasive ~1,600-nm fluorescence confocal imaging in the NIR-IIb window. (*A*) A schematic drawing illustrating in vivo confocal imaging of the mouse through the skin. (*B* and *C*) In vivo fluorescence confocal imaging of mouse hind limb vessels at a depth of ~270 μm after i.v. injection of PEG-CSQDs. (*B*) 2,000 × 2,000 μm. (Scale bar: 500 μm.) (*C*) 300 μm × 300 μm. (Scale bar: 50 μm.) (*D*) Cross-sectional fluorescence intensity profile of the hind limb vessel marked in *C* with the FWHM of ~7.9 μm and S/B ratio of 6.3. (*E–H*) In vivo layer-by-layer fluorescence confocal imaging of tumor vessels over an area (2,500 × 2,500 μm) after an i.v. injection of PEG-CSQDs; z = 0 is defined as the position when NIR-IIb signal started to show up in tumor. (Scale bar: 500 μm.) (*I* and *J*) High-resolution fluorescence confocal imaging of tumor vessels at a depth of 180 μm. (*I*) 800 × 800 μm. (Scale bar: 200 μm.) (*J*) 300 × 300 μm. (Scale bar: 50 μm.) (*K*) Cross-sectional fluorescence intensity profile of the tumor vessel marked in *J* with the FWHM of ~9.2 and S/B ratio of 8.8. Confocal imaging experiment parameters: 785-nm laser, 1,500-nm long-pass filter, laser power ~40 mW, photomultiplier tube voltage of 600 V.

Zhang et al.

bright through confocal imaging, suggesting that the PEG-CSQDs are an excellent nanoprobe for noninvasive 3D in vivo fluorescence imaging of animal disease models.

Since blood supply plays a critical role in tumor formation and growth (54), high-resolution imaging of tumor vasculatures could lead to useful information on vessel density, morphology, lengths, branching ratios, and leakage behavior. Until now, multiphoton confocal microscopy was the only 3D fluorescence-based modality for in vivo tumor imaging, and it requires surgically implanting an optical window on the mouse (55). We were able to use PEG-CSQDs for noninvasive, one-photon, through-skin confocal imaging of mouse tumor vasculatures in NIR-IIb. The shaved C57BL/6 mouse inoculated with a xenograft MC38 tumor was injected with PEG-CSQDs through the tail vein (200 μL, 5 mg/mL). The vasculatures of tumor from the surface to the interior were resolved (Fig. 4 E–H, z = 0 is defined as the position when NIR-IIb signal started to show up in the tumor). In contrast to the compact and abundant vessels on the surface of tumor, the internal vessels became sparse, indicating the cell necrosis inside the tumor (52). Given the fact that the thickness of skin was ~0.5 mm, the in vivo confocal imaging of tumor vessels reached an actual imaging depth of ~1.2 mm.

We observed that, in the high-resolution confocal images recorded at a depth of ~180 μm (Fig. 4 I and J), tumor microvasculature showed disorganization and lack of the conventional hierarchy, which was obviously different from the blood vessels of normal tissue with organized and regular branching order (Fig. 4B). The cross-section intensity profile examined that the apparent width of the tumor vessel was 9.2 with an S/B ratio of 8.8 (Fig. 4K). Previously, in vivo one-photon confocal imaging of tissues in the <900-nm range was limited by light scattering, either relying on thin skin-covered areas, like ears and eyes, or requiring invasive surgical procedures to remove skin using dorsal skinfold chambers (1, 56). The bright NIR-IIb PEG-CSQDs offers the feasibility of noninvasive confocal imaging for deep tissues, opening an approach to micrometer-scale, high-resolution imaging at the millimeter tissue depths in vivo.

In Vivo Pharmacokinetics and Biodistribution of CSQDs. The toxicity and fate of foreign nanomaterials introduced into a body are of important concerns. To investigate the pharmacokinetics and biodistribution, PEG-CSQDs were i.v. injected into a mouse cohort. By collecting blood at time points ranging from 1 to 72 h p.i. and measuring the blood CSQDs concentration using inductively coupled plasma atomic absorption spectrometry (ICP-AAS), we derived a blood circulation half-life of ~7 h (Fig. 5A). Based on the DLS result, the fully hydrated hydrodynamic size of PEG-CSQDs was ~18.2 nm (*SI Appendix*, Fig. S5), far larger than the cutoff size of 5.5 nm for efficient urinary excretion (57, 58). We observed that PEG-CSQDs were gradually excreted with feces overtime (*SI Appendix*, Fig. S10), suggesting a biliary excretion pathway of CSQDs (59). During an observation period of 28 d, no mice died in test group, and there was no obvious difference in body weight between the PEG-CSQD–treated group and the control untreated group (Fig. 5B).

Generally, foreign substances, including nanomaterials, introduced into a body typically accumulate in the liver and other innate immune systems rich in macrophages (60, 61). If not cleared effectively, in vivo toxicity might occur, especially for the PEG-CSQD material due to the toxic Pb and Cd elements. To further quantify the in vivo biodistribution of PEG-CSQDs over time, the main organs of mice were collected at 2, 24, and 72 h (n = 3 per group) after CSQD injection for fluorescence imaging (*SI Appendix*, Fig. S11) and ICP-AAS measurement (Fig. 5C). After 2 h p.i., liver, heart, lungs, and spleen showed bright NIR-IIb fluorescence of CSQDs, with liver and spleen as the dominant organs for accumulating PEG-CSQDs at ~15.8 and 16.8 percentage of injection dosage per gram of tissue (% ID/g), respectively. Fluorescence signal in the liver decayed and the amount of CSQDs decreased to 6.4% ID/g at 24 h p.i. After 72 h, the residual CSQDs in most of the organs decreased appreciably, indicating effective clearance of CSQDs. We analyzed the feces
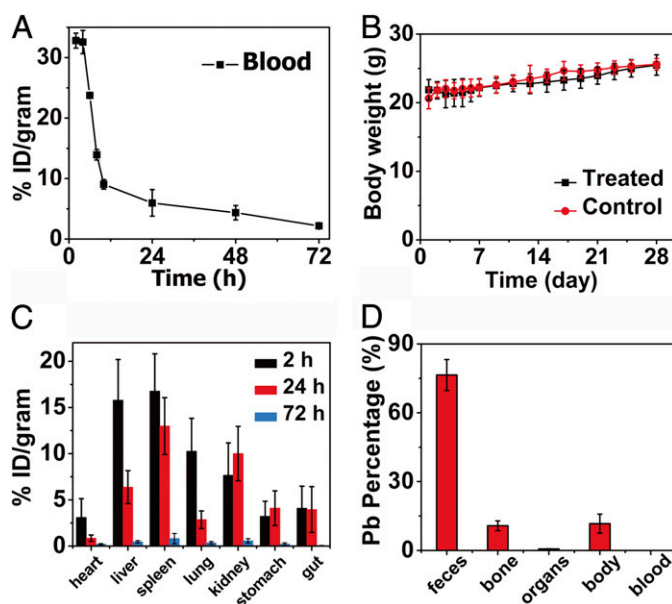

Fig. 5. In vivo pharmacokinetics and biodistribution of PEG-CSQDs. (*A*) Time course of CSQDs concentration in the blood of CSQDs treated mice over 72 h p.i., with a blood circulation half-life time of ~7 h. (*B*) Body weight of CSQDs-treated mice over a period time of 28 d. (*C*) Biodistribution of CSQDs in main organs of CSQDs-treated mice at 2, 24, and 72 h p.i. (*D*) Percentage of Pb in different parts of CSQDs-treated mice after 28 d p.i. All of feces during 28 d were collected. Organs: heart, liver, spleen, lungs, kidneys, stomach, and gut. Body: other parts of mouse, including skin, muscle, brain, et al.

of PEG-CSQDs–treated mice at 96 h p.i. and found that the amount of Pb in feces quickly reached a higher level at the time point of 24 h p.i., indicating the efficient clearance of CSQDs (*SI Appendix*, Fig. S12). We also collected all of the feces excreted from mice within 28 d p.i., measured them by inductively coupled plasma, and found that ~76% of injected CSQDs were excreted from the body with feces, whereas only 0.7% of injected CSQDs remained in seven main organs (Fig. 5D). In addition, we separated the CSQDs from feces using ultrasonication and centrifugation and characterized the supernatant by TEM. The CSQDs remained intact after being excreted through the biliary pathway, showing good in vivo stability of the probes (*SI Appendix*, Fig. S13). Overall, our study showed no obvious in vivo toxicity of the PEG-CSQDs and excretion of a majority within 1 mo of injection. The results suggested that the PEG-CSQDs are bright, 1,600-nm emitting probes highly useful for research with mouse models without toxicity problems through the ~1-mo period investigated.

Conclusion

In summary, we developed a bright fluorescent probe emitting on ~1,600 nm based on CSQDs and performed noninvasive in vivo fluorescence imaging with high temporal and spatial resolution in 2D wide-field and 3D confocal modes. Due to the core/shell structure and PEG layer, the CSQDs exhibited high aqueous stability and biocompatibility in physiological media and remained a high quantum yield, allowing for, in the NIR-IIb window, noninvasive, fast, real-time imaging of blood flows in mouse vasculatures. In vivo one-photon confocal imaging was realized in the NIR-IIb window using CSQDs, clearly resolving micrometer-scale capillaries at millimeter tissue depth with high S/B ratio. In vivo noninvasive 3D layer-by-layer confocal imaging of tumor reached a depth of ~1.2 mm using the CSQDs probe. Wide-field imaging of the tumor lighting up by enhanced permeation and retention effect reached a high T/NT ratio up to 32. It is also encouraging that the injected PEG-CSQDs were cleared from the main organs and excreted from the body through the biliary pathway, causing no obvious in vivo toxicity. This work led to a

Zhang et al.

www.manaraa.com

probe useful for deep tissue fluorescence imaging at the unusual 1,500- to 1,700-nm window for biomedical research.

Materials and Methods

The materials and methods used in this study are described in detail in *SI Appendix, Materials and Methods*. Information includes descriptions of CSQDs synthesis, surface modification and PEGylation, in vivo fluorescence imaging in 2D wide-field and 3D confocal modes, in vivo pharmacokinetics, and biodistribution of CSQDs. All animal experiments were performed under the approval of Stanford University's Administrative Panel on Laboratory Animal Care.

1. Ellenbroek SIJ, van Rheenen J (2014) Imaging hallmarks of cancer in living mice. *Nat Rev Cancer* 14:406–418.
2. Yang W, Yuste R (2017) *In vivo* imaging of neural activity. *Nat Methods* 14:349–359.
3. Hong G, Diao S, Antaris AL, Dai H (2015) Carbon nanomaterials for biological imaging and nanomedicinal therapy. *Chem Rev* 115:10816–10906.
4. Hong G, Antaris AL, Dai H (2017) Near-infrared fluorophores for biomedical imaging. *Nat Biomed Eng* 1:0010.
5. O'Connell MJ, et al. (2002) Band gap fluorescence from individual single-walled carbon nanotubes. *Science* 297:593–596.
6. Welsher K, et al. (2009) A route to brightly fluorescent carbon nanotubes for near-infrared imaging in mice. *Nat Nanotechnol* 4:773–780.
7. Welsher K, Sherlock SP, Dai H (2011) Deep-tissue anatomical imaging of mice using carbon nanotube fluorophores in the second near-infrared window. *Proc Natl Acad Sci USA* 108:8943–8948.
8. Hong G, et al. (2012) Multifunctional *in vivo* vascular imaging using near-infrared II fluorescence. *Nat Med* 18:1841–1846.
9. Hong G, et al. (2014) Ultrafast fluorescence imaging *in vivo* with conjugated polymer fluorophores in the second near-infrared window. *Nat Commun* 5:4206.
10. Hong G, et al. (2014) Through-skull fluorescence imaging of the brain in a new near-infrared window. *Nat Photonics* 8:723–730.
11. Hu F, et al. (2015) Real-time *in vivo* visualization of tumor therapy by a near-infrared-II Ag$_2$S quantum dot-based theranostic nanoplatform. *Nano Res* 8:1637–1647.
12. Diao S, et al. (2015) Fluorescence imaging *in vivo* at wavelengths beyond 1500 nm. *Angew Chem Int Ed Engl* 54:14758–14762.
13. Villa I, et al. (2015) 1.3 μm Emitting SrF$_2$:Nd^{3+} nanoparticles for high contrast *in vivo* imaging in the second biological window. *Nano Res* 8:649–665.
14. Dang X, et al. (2016) Layer-by-layer assembled fluorescent probes in the second near-infrared window for systemic delivery and detection of ovarian cancer. *Proc Natl Acad Sci USA* 113:5179–5184.
15. Franke D, et al. (2016) Continuous injection synthesis of indium arsenide quantum dots emissive in the short-wavelength infrared. *Nat Commun* 7:12749.
16. Antaris AL, et al. (2016) A small-molecule dye for NIR-II imaging. *Nat Mater* 15:235–242.
17. Antaris AL, et al. (2017) A high quantum yield molecule-protein complex fluorophore for near-infrared II imaging. *Nat Commun* 8:15269.
18. Bruns OT, et al. (2017) Next-generation in vivo optical imaging with short-wave infrared quantum dots. *Nat Biomed Eng* 1:0056.
19. Zhu S, et al. (2017) Molecular imaging of biological systems with a clickable dye in the broad 800- to 1,700-nm near-infrared window. *Proc Natl Acad Sci USA* 114:962–967.
20. Zhong Y, et al. (2017) Boosting the down-shifting luminescence of rare-earth nanocrystals for biological imaging beyond 1500 nm. *Nat Commun* 8:737.
21. Wang X, et al. (2018) Single ultrasmall Mn^{2+}-doped NaNdF$_4$ nanocrystals as multimodal nanoprobes for magnetic resonance and second near-infrared fluorescence imaging. *Nano Res* 11:1069–1081.
22. Zhu S, et al. (2018) 3D NIR-II molecular imaging distinguishes targeted organs with high-performance NIR-II bioconjugates. *Adv Mater* 30:e1705799.
23. Wan H, et al. (2018) A bright organic NIR-II nanofluorophore for three-dimensional imaging into biological tissues. *Nat Commun* 9:1171.
24. Naczynski DJ, et al. (2013) Rare-earth-doped biological composites as *in vivo* shortwave infrared reporters. *Nat Commun* 4:2199.
25. Wang R, Li X, Zhou L, Zhang F (2014) Epitaxial seeded growth of rare-earth nanocrystals with efficient 800 nm near-infrared to 1525 nm short-wavelength infrared downconversion photoluminescence for in vivo bioimaging. *Angew Chem Int Ed Engl* 53:12086–12090.
26. Hines MA, Scholes GD (2003) Colloidal PbS nanocrystals with size-tunable near-infrared emission: Observation of post-synthesis self-narrowing of the particle size distribution. *Adv Mater* 15:1844–1849.
27. McDonald SA, et al. (2005) Solution-processed PbS quantum dot infrared photodetectors and photovoltaics. *Nat Mater* 4:138–142.
28. Tang J, et al. (2011) Colloidal-quantum-dot photovoltaics using atomic-ligand passivation. *Nat Mater* 10:765–771.
29. Weidman MC, Beck ME, Hoffman RS, Prins F, Tisdale WA (2014) Monodisperse, air-stable PbS nanocrystals via precursor stoichiometry control. *ACS Nano* 8:6363–6371.
30. Zhao H, Wang D, Chaker M, Ma D (2011) Effect of different types of surface ligands on the structure and optical property of water-soluble PbS quantum dots encapsulated by amphiphilic polymers. *J Phys Chem C* 115:1620–1626.
31. Moroz P, et al. (2014) Infrared emitting PbS nanocrystal solids through matrix encapsulation. *Chem Mater* 26:4256–4264.
32. Supran GJ, et al. (2015) High-performance shortwave-infrared light-emitting devices using core-shell (PbS-CdS) colloidal quantum dots. *Adv Mater* 27:1437–1442.
33. Jin L, et al. (2016) Engineering interfacial structure in "Giant" PbS/CdS quantum dots for photoelectrochemical solar energy conversion. *Nano Energy* 30:531–541.
34. Neo DCJ, et al. (2014) Influence of shell thickness and surface passivation on PbS/CdS core/Shell colloidal quantum dot solar cells. *Chem Mater* 26:4004–4013.
35. Nakane Y, Tsukasaki Y, Sakata T, Yasuda H, Jin T (2013) Aqueous synthesis of glutathione-coated PbS quantum dots with tunable emission for non-invasive fluorescence imaging in the second near-infrared biological window (1000–1400 nm). *Chem Commun (Camb)* 49:7584–7586.
36. Sasaki A, et al. (2015) Recombinant protein (EGFP-Protein G)-coated PbS quantum dots for *in vitro* and *in vivo* dual fluorescence (visible and second-NIR) imaging of breast tumors. *Nanoscale* 7:5115–5119.
37. Zhao H, Chaker M, Ma D (2011) Effect of CdS shell thickness on the optical properties of water-soluble, amphiphilic polymer-encapsulated PbS/CdS core/shell quantum dots. *J Mater Chem* 21:17483–17491.
38. Jin T, Imamura Y (2016) Applications of highly bright PbS quantum dots to non-invasive near-infrared fluorescence imaging in the second optical window. *ECS J Solid State Sci Technol* 5:R3138–R3145.
39. Cademartiri L, et al. (2006) Multigram scale, solventless, and diffusion-controlled route to highly monodisperse PbS nanocrystals. *J Phys Chem B* 110:671–673.
40. Moreels I, et al. (2011) Size-tunable, bright, and stable PbS quantum dots: A surface chemistry study. *ACS Nano* 5:2004–2012.
41. Rivest JB, Jain PK (2013) Cation exchange on the nanoscale: An emerging technique for new material synthesis, device fabrication, and chemical sensing. *Chem Soc Rev* 42:89–96.
42. Neo MS, Venkatram N, Li GS, Chin WS, Ji W (2010) Synthesis of PbS/CdS core-shell QDs and their nonlinear optical properties. *J Phys Chem C* 114:18037–18044.
43. Kovalenko MV, Schaller RD, Jarzab D, Loi MA, Talapin DV (2012) Inorganically functionalized PbS-CdS colloidal nanocrystals: Integration into amorphous chalcogenide glass and luminescent properties. *J Am Chem Soc* 134:2457–2460.
44. Pellegrino T, et al. (2004) Hydrophobic nanocrystals coated with an amphiphilic polymer shell: A general route to water soluble nanocrystals. *Nano Lett* 4:703–707.
45. Zhang M-X, Huang B-H, Sun X-Y, Pang D-W (2010) Clickable gold nanoparticles as the building block of nanobioprobes. *Langmuir* 26:10171–10176.
46. Semonin OE, et al. (2010) Absolute photoluminescence quantum yields of IR-26 dye, PbS, and PbSe quantum dots. *J Phys Chem Lett* 1:2445–2450.
47. Murphy JE, et al. (2006) PbTe colloidal nanocrystals: Synthesis, characterization, and multiple exciton generation. *J Am Chem Soc* 128:3241–3247.
48. Fang J, Nakamura H, Maeda H (2011) The EPR effect: Unique features of tumor blood vessels for drug delivery, factors involved, and limitations and augmentation of the effect. *Adv Drug Deliv Rev* 63:136–151.
49. Hansen AE, et al. (2015) Positron emission tomography based elucidation of the enhanced permeability and retention effect in dogs with cancer using copper-64 liposomes. *ACS Nano* 9:6985–6995.
50. Wang AZ (2015) EPR or no EPR? The billion-dollar question. *Sci Transl Med* 7:294ec112.
51. Yuan F, et al. (1995) Vascular permeability in a human tumor xenograft: Molecular size dependence and cutoff size. *Cancer Res* 55:3752–3756.
52. Kobayashi H, Watanabe R, Choyke PL (2014) Improving conventional enhanced permeability and retention (EPR) effects; what is the appropriate target? *Theranostics* 4:81–89.
53. Diao S, et al. (2015) Biological imaging without autofluorescence in the second near-infrared region. *Nano Res* 8:3027–3034.
54. Tozer GM, Kanthou C, Baguley BC (2005) Disrupting tumour blood vessels. *Nat Rev Cancer* 5:423–435.
55. Tozer GM, et al. (2005) Intravital imaging of tumour vascular networks using multi-photon fluorescence microscopy. *Adv Drug Deliv Rev* 57:135–152.
56. Marques PE, et al. (2015) Imaging liver biology *in vivo* using conventional confocal microscopy. *Nat Protoc* 10:258–268.
57. Choi HS, et al. (2007) Renal clearance of quantum dots. *Nat Biotechnol* 25:1165–1170.
58. Peng C, et al. (2017) Targeting orthotopic gliomas with renal-clearable luminescent gold nanoparticles. *Nano Res* 10:1366–1376.
59. Zhao L, et al. (2016) Silica–polymer hybrid with self-assembled PEG corona excreted rapidly via a hepatobiliary route. *Adv Funct Mater* 26:3036–3047.
60. Smith BR, et al. (2014) Selective uptake of single-walled carbon nanotubes by circulating monocytes for enhanced tumour delivery. *Nat Nanotechnol* 9:481–487.
61. Weissleder R, Nahrendorf M, Pittet MJ (2014) Imaging macrophages with nanoparticles. *Nat Mater* 13:125–138.

Zhang et al.

CHEMISTRY

www.manaraa.com